Lithospheric Thickness of Volcanic Rifting Margins: Constraints From Seaward Dipping Reflectors

Xiaochuan Tian[1,2] and **W. Roger Buck[1]**

[1]Lamont-Doherty Earth Observatory, Columbia University, Palisades, NY, USA, [2]School of Earth Science and Geological Engineering, Sun Yat-sen University, Guangzhou, China

Abstract Seaward dipping reflectors (SDRs) are large piles of seaward thickening volcanic wedges imaged seismically along most rifted continental margins. Despite their global ubiquity, it is still debated whether the primary cause of SDR formation is tectonic faulting or magmatic loading. To study how SDRs might form, we developed the first two-dimensional thermomechanical model that can account for both tectonics and magmatism development of SDRs during rifting. We focus here on the magmatic loading mechanism and show that the shape of SDRs may provide unprecedented constraints on lithospheric strength at volcanic rifting margins. For mapping SDRs geometries to lithospheric strength, a sequence of model lithospheric rheologies are treated, ranging from analytic thin elastic plates to numerical thick elasto-visco-plastic crust and mantle layers with temperature and stress-dependent viscosity. We then analyzed multichannel seismic depth-converted images of SDRs from Vøring and Argentinian rifted margins in terms of geometric parameters that can be compared to our model results. This results in estimates for the lithospheric thickness during rifting at the two margins of 3.4 and 5.7 km. The plate thickness correlates inversely with mantle potential temperature at these margins during rifting, as estimated by independent studies.

1. Introduction

Mounting evidence indicates that intensive volcanism occurs during most continental breakup events and before seafloor spreading (Buiter & Torsvik, 2014; Courtillot et al., 1999; Hinz, 1981; Kendall et al., 2005). As voluminous as continental flood basalts, seaward dipping reflectors, or SDRs, are large igneous wedges emplaced at continent-ocean boundaries that are now buried under kilometers of postrift sediments. They are seen in multichannel seismic (MCS) reflection profiles as reflectors dipping seaward. Drilling indicates SDRs consist of thin layers of sediments interbedded within thicker layers of lava (Eldholm et al., 1995). SDR wedges generally feature downdip thickening and their dip angle increases with depth (Jackson et al., 2000; Mutter et al., 1982; Paton et al., 2017; Figure 1). Globally, SDRs appear to be several to tens of kilometers thick, up to hundreds of kilometers wide (across margin) and several thousand kilometers long (along margin; McDermott et al., 2018).

Hinz (1981) first presented a global compilation of MCS profiles with SDRs. Following him, many authors have reported observations of SDRs including along North Atlantic margins (e.g., Mutter et al., 1982; Planke & Eldholm, 1994), South Atlantic margins (e.g., Elliott et al., 2009; Franke et al., 2010; Gladczenko et al., 1998), Indian margins (e.g., Calvès et al., 2011), Australian margins (e.g. Direen & Crawford, 2003), and Antarctica margins (e.g., Kalberg & Gohl, 2014; Kristoffersen et al., 2014). Tilted lava packages on Iceland (Bodvarsson & Walker, 1964) and parts of the Deccan traps (Watts & Cox, 1989) are on-land SDRs analogues.

There are two very different hypotheses for the formation of SDRs: tectonic faulting or magmatic loading. The major difference is how to make the accommodation space for infilling volcanic lava flows to form the SDRs. Many authors interpret SDRs as bounded by landward dipping, large-offset normal faults with the downward deflection of the hanging wall producing the "accommodation space" for syntectonic volcanics (Becker et al., 2016; Geoffroy, 2005; Gibson & Love, 1989; Pindell et al., 2014; Planke et al., 2000; Quirk et al., 2014). Most on-land regions with massive volcanic piles show little evidence of large-offset normal faulting. Also, in most areas of continental and oceanic plate separation the normal faults dip oceanward. However, in an effort to numerically simulate SDR formation, Geoffroy et al. (2015) produce landward dipping faults with a particular set of preexisting weak zones, and not including effects of magma intrusion or lava infilling.
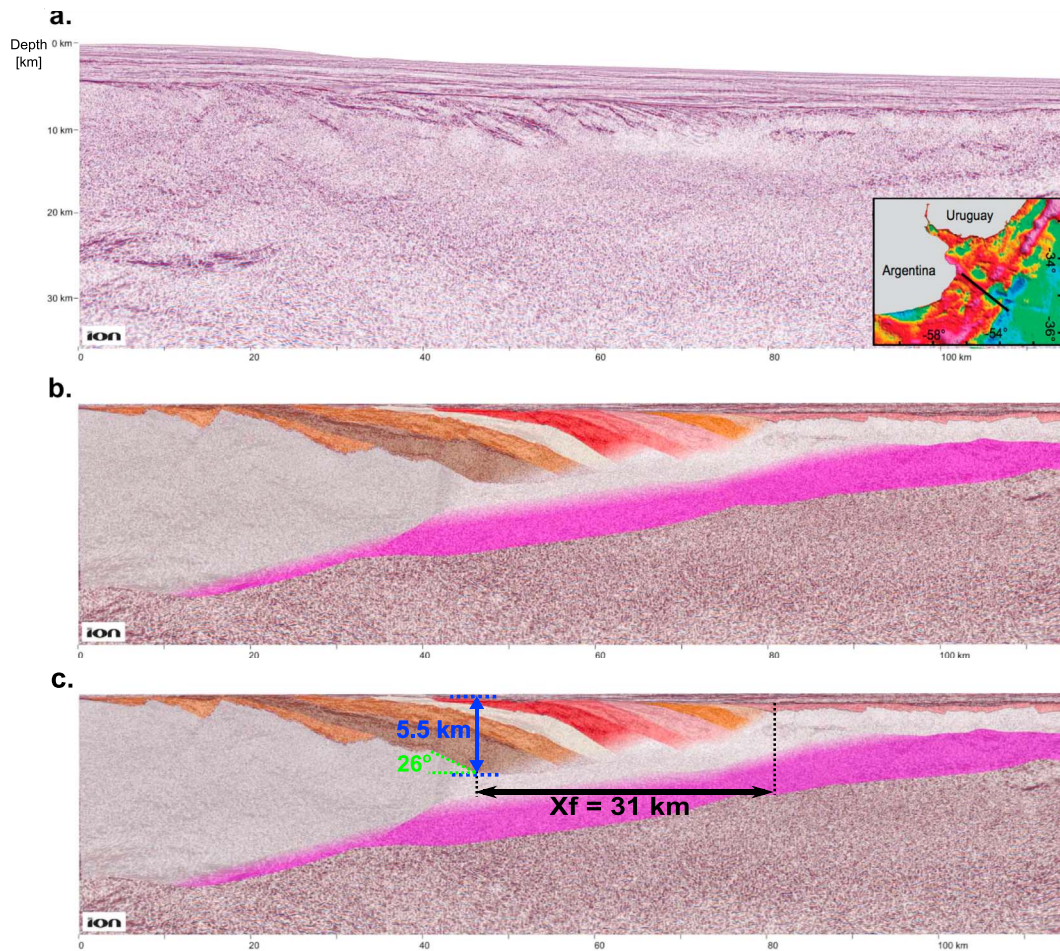
Figure 1. Multichannel seismic data of SDRs example offshore Argentina centered at 55°W, 35°S (from Paton et al., 2017). (a) Uninterpreted prestack depth migrated data image. (b) From (a), but with sediment layers removed and the SDRs surface flattened. Each SDR wedge is colored. (c) Marked version of panel b. X_f is 31 km and is the horizontal distance between the tip of the flat SDR and tip of the SDR that has the largest dip angle of 26°. The SDR wedges are 5.5 km thick. SDR = seaward dipping reflector.

Magmatic loading to produce dipping lava beds was first proposed by Bodvarsson and Walker (1964), who suggested that subsidence due to volcanic loading combined with crustal drift can explain the geometry of flow units on Iceland. Within the framework of plate tectonics, Palmason (1973) proposed a kinematic model for crustal generation at Iceland assuming parabolic functions for describing the extension and subsidence velocities of lava piles. Paton et al. (2017) suggests that variable SDR packages indicate changing magma supply. Buck (2017) developed an analytical model of SDR formation assuming the elastic thin plate approximation for plate flexure due to the volcanic and magmatic loading. With reasonable values of flexural wavelength and dike height, the model produces SDRs that are shaped much like those observed (Figures 2 and 3). With either jumps in the axis of diking or oscillations in extrusion, the model can generate the kinds of multiple SDRs wedges sometimes observed (e.g., Becker et al., 2016).

The analytic model successfully explains many observations, yet it makes several simplifying approximations. To permit a closed-form solution, it assumes the lava covers the whole plate surface. However, lava flows should be restricted spatially to low-lying regions adjacent to the spreading center. Morgan and Watts (2018) model SDR formation by applying finite difference method (FDM) to solve the general thin plate flexure equation that allows spatial and temporal variability in plate strength and magmatic loading. They constrain their model results with seismic and gravity anomaly data and find that it requires a broken plate boundary condition and temporally decreasing effective elastic plate thickness to fit such observations. Both the analytic and the FDM models assume elastic thin plate and cannot
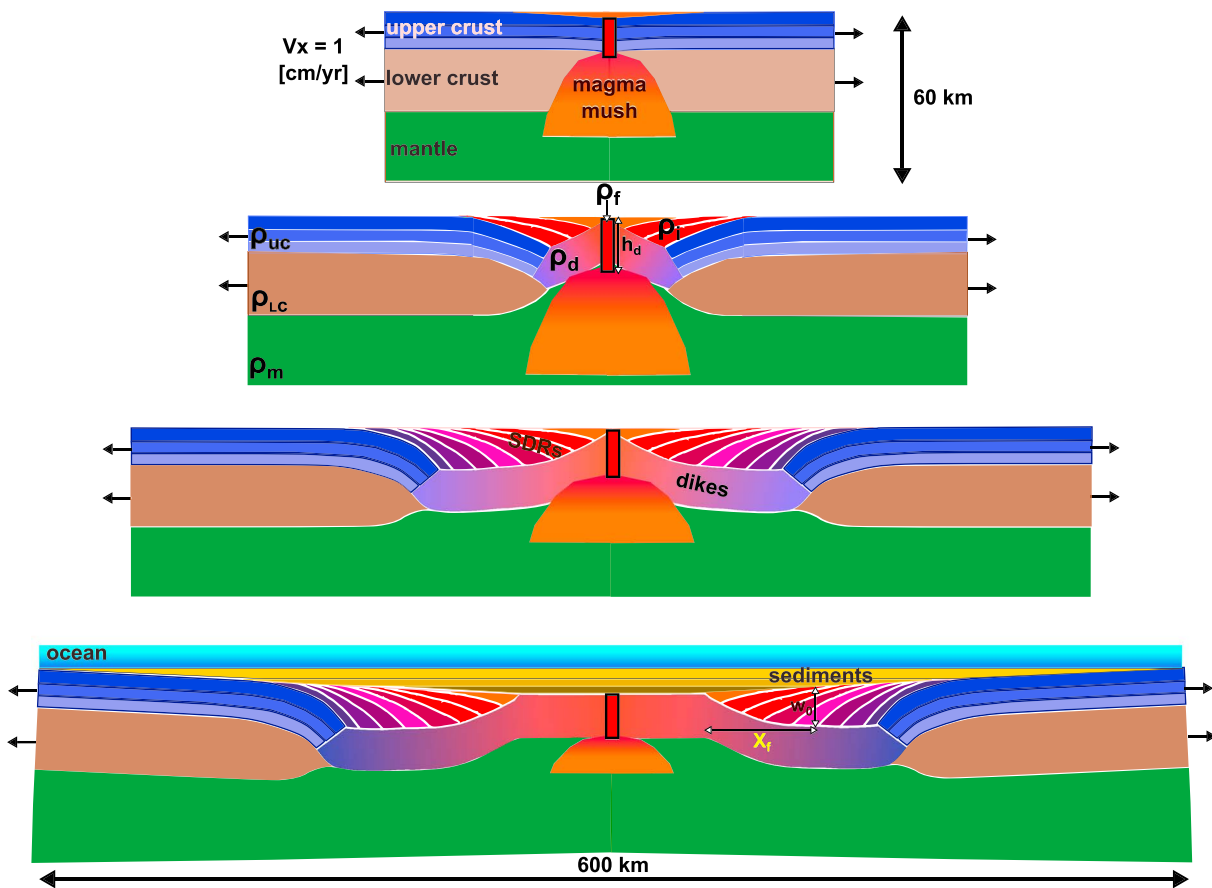
Figure 2. Cartoon illustration of SDRs formation processes. The SDRs geometries are extracted from results of 2-D numerical models. The intrusion of magma as a dike in the top panel provides a load on the lithosphere as the dike solidifies and so increases in density. Volcanic flows fill in the region of subsidence driven by the dike load and further loads the lithosphere. The middle panel shows the effect of multiple cycles of dike intrusion, solidification, and volcanic infill. The bottom panel shows how the volcanics eventually subside and are covered with sediment as more normal seafloor spreading occurs. SDR = seaward dipping reflector.

consider the lithosphere as a thick plate composed of realistic materials with evolving density and thermal-mechanical structures.

Here, we develop two-dimensional numerical models to simulate SDRs formation in the context of continental rifting. The model formulation allows spatially varying lava infill (Abdelmalak et al., 2016), lower crustal underplating (Saikia et al., 2017; White et al., 2008), and elasto-visco-plastic (EVP) rheology (Brace & Kohlstedt, 1980; Goetze & Poirier, 1978; Shelton & Tullis, 1981) both with and without thermal evolution.

Lithospheric strength at a rifting center is likely to exert a major control on the crustal structures formed during continental breakup. It is also essential for determining whether or not a rift will succeed to seafloor spreading (e.g., Bialas et al., 2010; Buck, 2006). Common methods for studying lithospheric strength using gravity and topography data that gives current plate strength may not be accurate for plate boundaries during ancient rifting (e.g., Ebinger & Hayward, 1996; Pérez-Gussinyé et al., 2007) because those signals could have changed since rifting as the plate cools down and is loaded with postrift sediments. However, as we will show, the shape of magmatic loading formed SDRs is a direct expression of the plate strength during rifting and should change little following their formation. Recent workers (McDermott et al., 2018; Paton et al., 2017) argue that near-shore (or type 1) SDRs result from tectonic processes while offshore (or type 2) SDRs are formed by magmatic processes. The numerical models we develop can treat both tectonic and magmatic processes, but here we focus on the effects of magmatic loading and leave the complexities of faulting for future investigations. The major goal of this study is to provide a mapping between the geometry
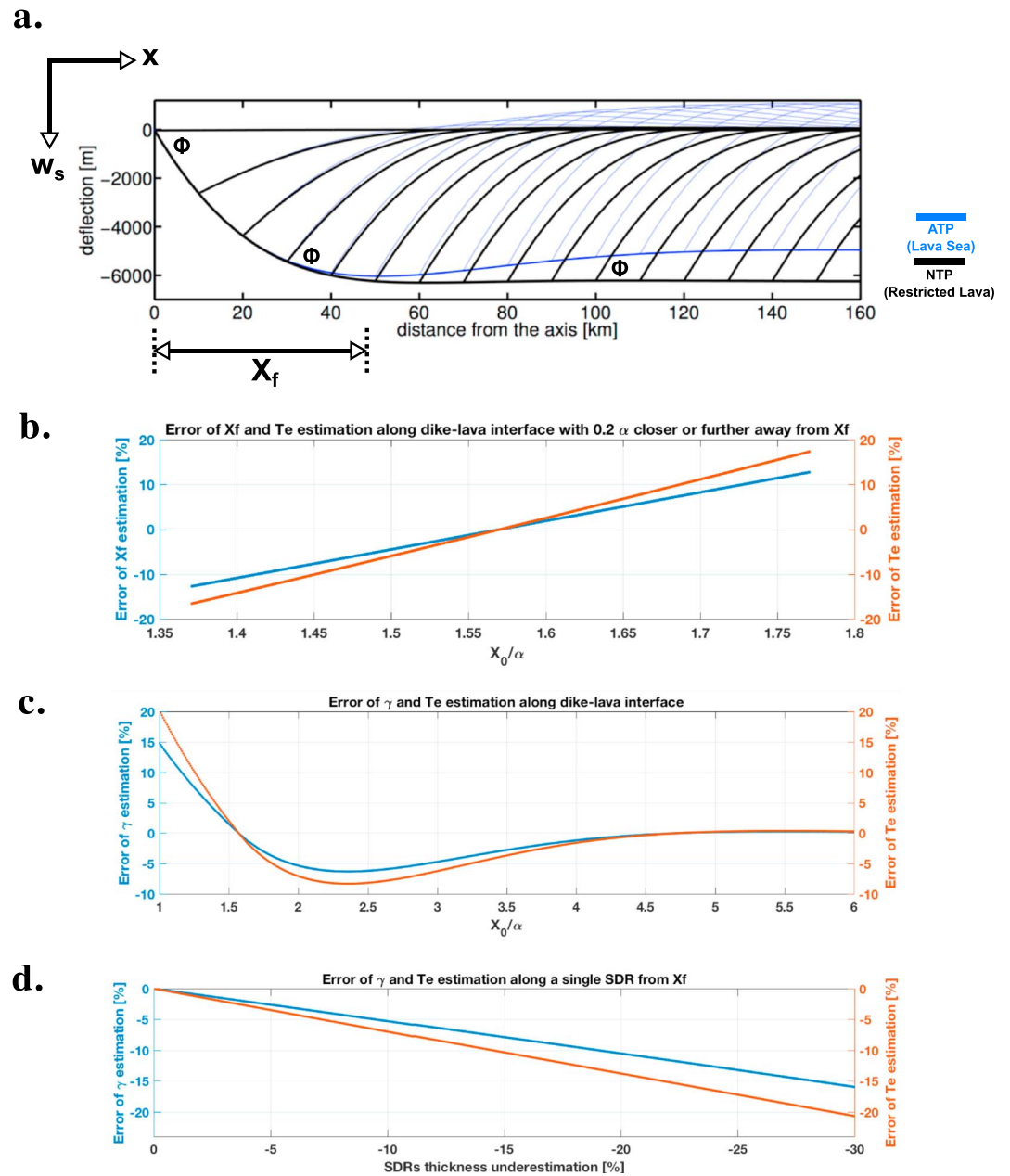
Figure 3. (a) Direct comparison between ATP and NTP with $h_d = T_e = 5$ km. Blue lines are for ATP "lava sea" results. X_f is the horizontal distance between the tip of flat SDR and the SDR that has developed to a steady shape. ϕ is the angle between the tip of each SDR and the dike-lava interface. The vertical exaggeration is 7 to highlight the difference in the models. (b) Analytic error estimation of X_f and T_e if measuring along the dike-lava interface. (c) Analytic error estimation of γ and T_e if measuring along the dike-lava interface. (d) Analytic error estimation if missing lower part of the SDR wedges. ATP = analytic elastic thin plate; NTP = numerical thin plate; SDR = seaward dipping reflector.

of magmatic loading-controlled SDRs and lithospheric strength, or thickness, during their formation at volcanic rifted margins.

2. Models and Results

We build a sequence of models that begin with the simplest possible treatments for lithospheric response under magmatic loadings during the last stage of continental rifting, at which SDR forming transitions to

seafloor spreading (Figure 2). We progressively reduce assumptions and show the effects of those changes, beginning with a brief description of an existing analytic model and culminating with a fully 2-D thermal-mechanical model of volcanic margin evolution. This effort is divided into six steps: First, we review the analytic thin plate flexure formulation and describe how its prediction can be related to observations. Second, we apply FDMs to numerical thin plate (NTP) models with spatially restricted lava flow. Third, we show how 2-D thick plate models converge with increasing numerical resolution and the results are compared with NTP models. Fourth, we develop long-term 2-D numerical models with elastic-plastic (EP) rheology to quantify the effects of plasticity. Fifth, we use the long-term 2-D numerical models with constant thermal structure to quantify the effects of EVP rheology. Sixth, we describe models which the thermal evolution affects the strength of the lithosphere, and we show the effects of different crustal rheologies and amounts of underplating.

2.1. Review of Analytic Elastic Thin Plate Model and Its Linkage to SDRs Observations

According to a number of workers (e.g., Bodvarsson & Walker, 1964; Morgan & Watts, 2018; Watts & Cox, 1989), SDRs geometries are an expression of the flexural response of a lithosphere due to magmatic loads. An analytic description of the magma loading model, derived by Buck (2017), depends on two length scales. The vertical scale is

$$w_0 = h_d \frac{\left(\rho_d - \rho_f\right)}{\left(\rho_c - \rho_i\right)}$$

where h_d is the height of the dike, ρ_d is the density of the solidified dike, ρ_f is the density of the fluid magma filling the dike, ρ_c is the density of the compensating lower crustal or mantle material that flows in response to lateral load variations, and ρ_i is the density of the volcanic or sedimentary material infilling the depression produced by the load of the dike. The fluid magma-filled dike is assumed to rise so that it is in local isostatic equilibrium. For simplicity, in the analytic model, the upper crust is taken to have an initial thickness of h_d and have the same density ρ_f as the fluid magma in the dike. This insures that the dike rises to the level of the initial top of the crust. The horizontal scale of bending of the model SDRs depends on the flexure parameter α, and for a thin elastic plate, this is proportional to $Te^{3/4}$ where T_e is the effective elastic plate thickness.

The analytic description of magmatic loading produces model geometries that are similar to real SDR packages. To relate real SDR geometry to the effective elastic thickness of this model, we define three simple and potentially observable parameters. First, we define X_f as the horizontal distance between the tip of the last deposited lava infill and the first place where the dike-lava interface is flat (Figures 2 and 3a). As derived in the supporting information this distance is $\pi\alpha/2$. It may be difficult to accurately determine in data either the place of the last axis of diking before seafloor spreading or the place where the dike-lava interface becomes flat. Uncertainty in this horizontal position of $\pm 0.2\alpha$ ($\pm 13\%$ of X_f) results in a T_e estimation error of less than 20% (Figure 3b).

We also consider the ratio γ between the thickness of the SDR and the slope of the flows intersecting with the dike-lava interface. As noted in the supporting information this ratio varies slowly with distance from the axis of diking and equals $\alpha/2[1+ \exp(-\pi/2)]$ at a distance X_f away from the seaward tip of the last deposited SDR. Uncertainty in the horizontal position of X_f from α to 5α away from the tip of the flat SDR results in an estimation error of T_e ranges from $+20\%$ to -10% (Figure 3c). The effect of underestimating the depth to the base of the SDRs, due to difficulties in imaging the deeper SDRs, by 30% produces an underestimate of T_e of ~20% (Figure 3d).

The last way of relating SDR geometry to model parameters is through the angle ϕ between the dike-flow interface and the intersecting flow (SDR; see Figure 3a). This is the easiest measurement to make on seismic depth sections and has the advantage that the analytic model predicts that the angle is nearly constant with distance from the axis of diking. As described in the suppporting information (equations (6) and (7)), it depends on both w_0 and α. As long as we can estimate the thickness of the entire SDR package (~w_0), we can relate this angle to the effective elastic thickness of the lithosphere.

Before we relate seismic data on SDRs to model predictions, we will consider how the approximations that go into the analytic model affect the parameters X_f, γ and ϕ. We will show that these parameters are useful

for comparing the analytic model geometry to that predicted by less approximate numerical models. Using these three observables, X_f, γ and ϕ, we can reliably link SDRs geometries from MCS data to the plate strength that supports the SDRs in terms of effective elastic thickness T_e and lithospheric thickness H_L.

2.2. Numerical Elastic Thin Plate Model (NTP)

To get a closed-form description of the model geometry, the analytic model treats the flexural response to magmatic loads as if lava flows cover the whole surface. However, lava should only fill in the region deeper than the top of the axial dike (Figure 2). To remove this inconsistency, we show the effects of more realistic lava loading on SDRs geometries while still using the thin plate flexure approximation. The FDM is used to solve for the vertical deflections due to the load of a half-dike added to the end of a thin elastic plate. The region adjacent to the axis that are deflected below their initial positions are then effectively filled with volcanic lava. The load of that infilling lava is then added to the plate and the resulting deflections computed. New lava is added to keep the volcanic surface at the initial surface level and the process is iterated until a steady state is achieved. The accretion of additional dikes produces the same plate deflections and infill as the first dike and so the shape of model volcanic packages can be easily calculated (see supporting information for details).

This NTP model depends only on two scales: the flexure parameter α and the maximum thickness w_0. The NTP model results in a much smaller off-axis bulge than for the analytic model with the same values of α and w_0 (Figure 3a). This occurs because when the plate is flexed upward off-axis into the air, compensating mantle or lower crust resists being pulled up more than it would if the surface moved up into fluid with the density of lava. Compared to the analytic models with the same parameters, the NTP models predict that X_f is ~20% larger, γ is ~6% larger and ϕ is about the same.

2.3. Two Dimensional Numerical Models

The large magnitude curvature of SDRs implies that the elastic tensional stress near the surface can cause plastic yielding and the elastic thin plate approximation may be inaccurate. We simulate deformation of finite thickness lithosphere in response to magmatic loads using the numerical code FLAC (Fast Lagrangian Analysis of Continua; Buck et al., 2005; Cundall, 1989). This approach allows us to consider the effects of elastic and nonelastic deformation including viscous flow and brittle-plastic deformation. FLAC is a two-dimensional explicit hybrid finite element-finite difference code that solves continuity, momentum balance, and heat equations. This code has been used to model strain localization for faulting in both two and three dimensions with and without sedimentation (Choi et al., 2008; Choi et al., 2013; Tian & Choi, 2017) and to track heat advection and diffusion (Lavier & Buck, 2002). In order to simulate and quantify lava infill, we modify the code to track surface deflections and add lava elements accordingly similar to Choi et al. (2013). Higher-resolution tracers (described in the supporting information) are deployed at the surface at set time intervals and move according to the velocity field. These tracers allow more precise quantification of the SDR geometry.

We only simulate the right half of a symmetric volcanic rift to save computation time. The bottom boundary is a Winkler foundation with the compensation pressure defined at the bottom of the rightmost column. Both the right and left boundaries are shear stress free. The horizontal velocity of the right boundary is set to be 1 cm/year. The left boundary is treated in either of two ways that approximate a broken plate. For EP thick plate models, we set a lithostatic normal stress and new dike material is accreted during periodic remeshing. For EVP models that account for variable viscosity, a column of low viscosity "dike elements" is made to widen steadily while the horizontal boundary velocity is set to 0.

For the simpler cases we use either a single elastic or EP layer with density of upper crust of 2,800 kg/m^3 supported by Winker foundation of lower crust with density of 3,000 kg/m^3. In the EVP cases, layers with both upper and lower crust are assumed to float on an underlying mantle layer. Brittle deformation is calculated with a Mohr-Coulomb failure criterion with a constant friction angle of 30°, and cohesion of 20 or 40 MPa. Ductile deformation follows Newtonian or non-Newtonian rheology with flow rules of dry quartz (Brace & Kohlstedt, 1980; Davis & Lavier, 2017) or dry plagioclase (Shelton & Tullis, 1981) for the crust and dry Olivine (Goetze & Poirier, 1978) for the mantle. Constant thermal structure models assume linearly increasing temperature with depth. We vary initial crustal thickness and bottom boundary temperature

conditions for simulating different mechanical thickness and dike loads. The crustal thickness controls effects of dike loads, while bottom temperature affects initial mechanical thickness and thus the plate strength.

For thermally evolving models, we include a mantle layer underlying the crust. Diking brings in heat by intruding 1300 °C fluid dikes that has latent heat of solidification of 500 kJ/kg following Behn and Ito (2008). Meanwhile, cooling due to hydrothermal circulation is approximated by enhancing the thermal conductivity via Nusselt number in regions shallower than 10 km and colder than 600 °C. Nusselt number is assumed to increase linearly from 5 to 8 with plastic strain from 0 to 1.

2.3.1. Numerical Convergence of Elastic and EP Thick Plate Cases

We first show how the 2-D model results depend on grid size and number of numerical iterations. Due to the nonlinearity of the problem and for the purpose of benchmarking, we only consider cases with a single large (i.e., 1 km wide) dike load (Figure S3a). The parameters used in the FLAC and corresponding NTP models are shown in Tables S1 and S2. The results obtained after sufficient numerical iterations that the deflection changes are insignificant (Figures S3b and S3c) show that elastic thick plate results are within 1% of the deflection of the NTP results. The slightly larger deflection for the thick plate cases are anticipated due to vertical compression (Comer, 1983). Results indicate (see Figures S3d and S4d) that decreasing the grid size below 1 km makes a negligible difference even for our thinnest lithospheric thickness of ~6 km. For simplicity, we keep this 1-km grid size for all our models. When subjected to this narrow load the EP thick plate model behaves much like its elastic thick plate counterpart (Figure S4) in terms of convergence but shows a relatively larger curvature due to plastic yielding (Figures S4b and S4c).

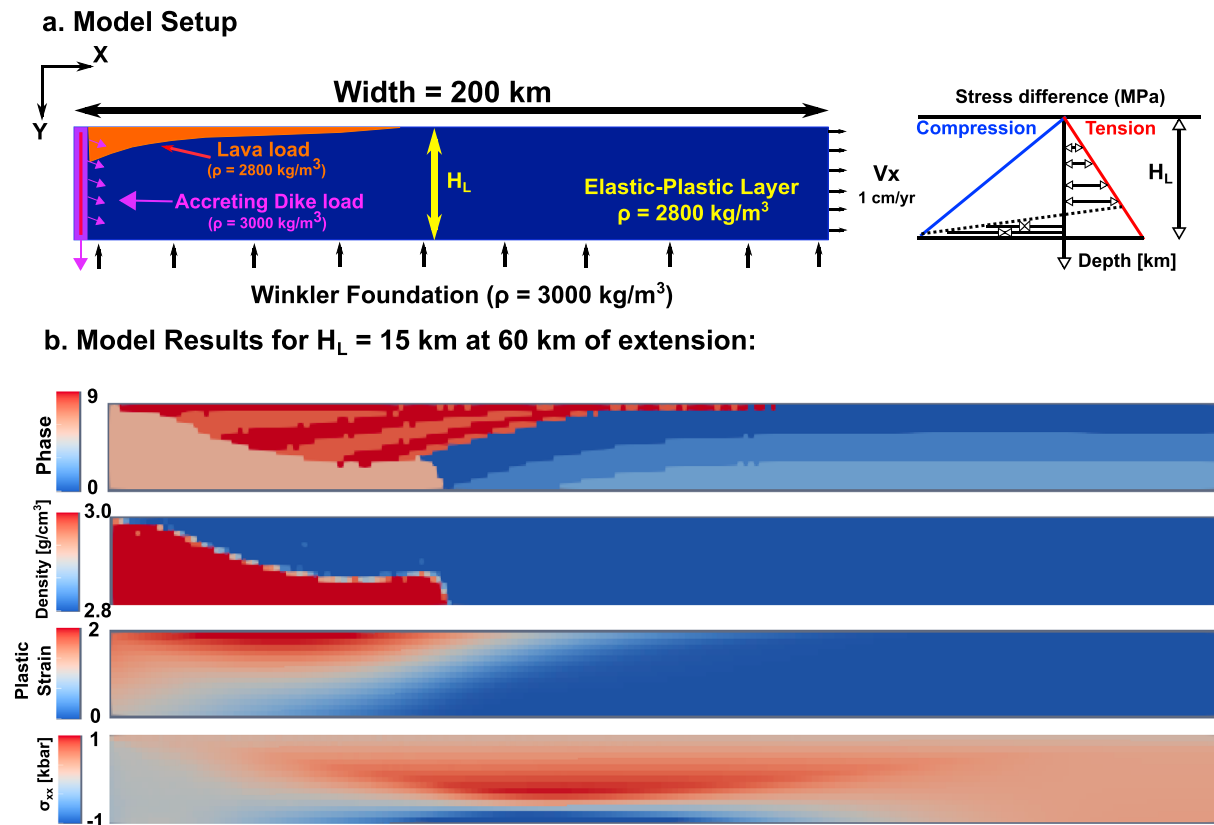### 2.3.2. EP Thick Plate With Long-Term Plate Extension

The analytic and NTP models assume invariable plate strength and lithospheric response with repeating magmatic loads. However, the system may have spatial and temporal changes in density structure, plate strength and magmatic loads. We here allow long-term plate motion away from the axis of dike accretion with plastic deformation and try to quantify these effects by considering the evolution of effective plate strength with geological time-averaged repeated small dike (i.e., Qin & Buck, 2008) and related volcanic loads.

In contrast to the previous benchmark, we treat constant dike widening at the rift axis and a constant horizontal velocity at the right boundary (Figure 4a). The low-density upper crust and volcanic infill dynamically changes. The plastic strain pattern (Figure 4b) follows the overall shape of the SDRs because new lava added to the surface with initially zero plastic strain deforms near the surface due to the plate bending and is advected with the plate. The major result of a range of model cases (Figure 5) is that the predicted flow geometry is similar to that of the analytic model, predicted by steady state deflection. Measuring X_f, γ, described in section 2.1, allows us to estimate the effective plate elastic thickness T_e for the analytic model that best fits the thick plate results. We vary the brittle layer thickness H_L and estimate the corresponding T_e (Figure 5b). Varying the layer cohesion from 20 to 40 MPa has little effect on the relation between H_L and T_e. The average effective elastic thickness from both X_f and γ varies with H_L according to the best linear fitting function $T_e = 0.49 H_L$ for models with cohesion of 20 MPa.

2.3.3. EVP Thick Plate With Constant Thermal Structure

The EP thick plate models neglect the effects of viscous flow that could alter the plate bending behavior (e.g., Olive et al., 2016). In this section, we assume a laterally uniform thermal structure with strain rate independent Newtonian rheology to quantify the effects of viscoplastic deformation. The viscosity η (Pa · s) is given by $\eta = \dot{\varepsilon}^{\frac{1}{n}-1} A^{-1/n} \cdot \exp(E/nRT) \cdot 10^6$ where $A = 500$ (MPa^{-n} · s^{-1}), $E = 2 \times 10^5$ (J/mol), $n = 1$ for Newtonian rheology, R is the universal gas constant of 8.31448 (J · mol^{-1} · K^{-1}), and T is the temperature in degrees Celsius.

Compared to the previous single-layer EP model, the EVP model with both upper and lower crust (Figure 6) allows us to treat a more realistic density structure where the lower density upper crust subsides into the higher density lower crust (Figure 6b). The lower density root exerting a local upward buoyancy force away from the axis, together with the downward loads from dikes near the axis, produces a bending moment that could further rotate the SDRs. The neutral plane where the stress difference due to bending is zero deepens significantly because of plasticity near the surface. The angle between the flows and the dike flow interface, ϕ, varies from 43° to 54° (Figure 7) are about 10° larger than the analytically predicted angle ϕ that ranges

Figure 4. Model results for elastoplastic thick plate with long-term extension. (a) Model setup: Model domain is H_L thick and 200 km wide. The elastic and plastic properties are defined in the text. (b). Seaward dipping reflector geometries (phase numbers are for different model materials, 1–3 are for upper crust; 4 for lower crust; 5 for mantle; 6 and 7 for dikes; 8 and 9 are for lava flows), density, plastic strain, and deviatoric horizontal stress at 60 km of extension.

from 30° to 43° (Figure S2). The torque due to upper crustal root along with viscous relaxation might contribute to this extra SDR rotation.

When the model reaches steady state, in which the pattern of deflections per amount of dike opening becomes stable, we measure X_f and γ to estimate effective α and T_e. We found systematic larger T_e from X_f estimation. The lithospheric thickness is defined as the distance from the surface to the depth where compressional horizontal deviatoric stress decreases to 5 MPa, similar to the base of the "mechanical boundary layer" when deformation transitions from elastic-brittle to viscous domination (Artemieva, 2011). The average effective elastic thickness from both X_f and γ varies with H_L according to the best linear fitting function $T_e = 0.32 \, H_L$ (Figure 7b), which is much less than that of the EP thick plate results (Figure 5b). This results from the rheology difference between the two. For the EP case, the maximum compression appears at the bottom of the plate (Figure 4b), whereas for the EVP case, the maximum differential stress (effectively the brittle ductile transition) is within the modeled layer and its depth depends on the curvature of the bending plate (Figure 6a). The integrated bending moment for EVP model with same H_L is thus much less than its EP model counterpart. Note that in the cases illustrated here the lower crust flows to compensate the magmatic loads. The overall trend of larger Te_{X_f} than Te_{γ} might be due to the extra bending moment exerted from the lower density upper crustal root, which gives a larger dip angle without changing other parameters.

2.3.4. EVP Thick Plate With Thermal Evolution

Thermal structure is taken as a control variable in previous models. However, magmatism brings heat to the rifting center, changing the thermal structure and plate strength. Here we show results of models that include heating due to dike intrusion of magma with an initial temperature of 1300 °C and latent heat of solidification as well as cooling from parameterized hydrothermal circulation. We test two crustal

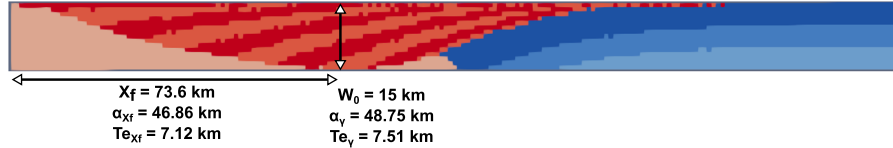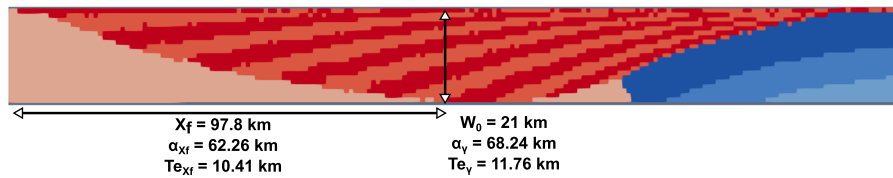## a. EP thick Plate with different H_L
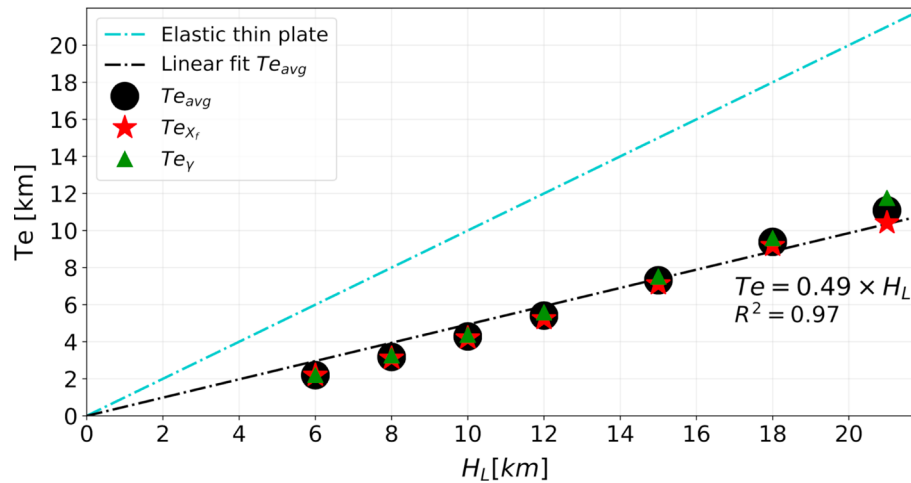
H_L = 10 km at 70 km of extension:

X_f = 49.5 km	W_0 = 10 km
α_{Xf} = 31.5 km	α_γ = 32.5 km
Te_{Xf} = 4.2 km	Te_γ = 4.37 km

H_L = 15 km at 100 km of extension:

X_f = 73.6 km	W_0 = 15 km
α_{Xf} = 46.86 km	α_γ = 48.75 km
Te_{Xf} = 7.12 km	Te_γ = 7.51 km

H_L = 21 km at 140 km of extension:

|	
X_f = 97.8 km	W_0 = 21 km
α_{Xf} = 62.26 km	α_γ = 68.24 km
Te_{Xf} = 10.41 km	Te_γ = 11.76 km

b. Model results for EP effective Te from X_f and γ

Figure 5. Model results for elastoplastic (EP) thick plates with different layer thickness H_L. (a) Predicted geometries at model times when the volcanic infill reaches the bottom boundary. $\phi \approx 30°$ (b) Estimated effective elastic thickness T_e for cases with different initial plate thicknesses H_L. The red stars are T_e estimated from X_f measurements, the green triangles are from γ measurements from the models, and the black dots are the average of the two estimations. The black dashed line is the best linear fit ($T_e = 0.49H_L$ with $R^2 = 0.97$) to the average T_e (black dots) that passes the origin.

rheologies (Figure 8): dry quartz (Brace & Kohlstedt, 1980) and dry plagioclase (Shelton & Tullis, 1981). We also study the effects of magma intrusion into the lower crust that may approximate magmatic underplating. For these cases, a mantle layer is included. The lava is deposited with a surface temperature of 0 °C because flows should cool within years.

The overall behavior is qualitatively similar to the previous constant thermal structure EVP models but varies in detail (Figures 8 and 9). The biggest difference is that diking provides heat that weakens the plate near the rifting center (Figure 8b). This leads to a reduction in brittle thickness on axis and thus the effective dike load near the axis decreases. However, this does not generate a large difference in the total thickness of the SDR package because as dense solidified dikes move off axis, they accrete to the colder off-axis lithosphere providing a downward load. The downward advection of cold volcanic infill produces minor thickening of lithosphere within a flexural wavelength the axis (Figure 8b).
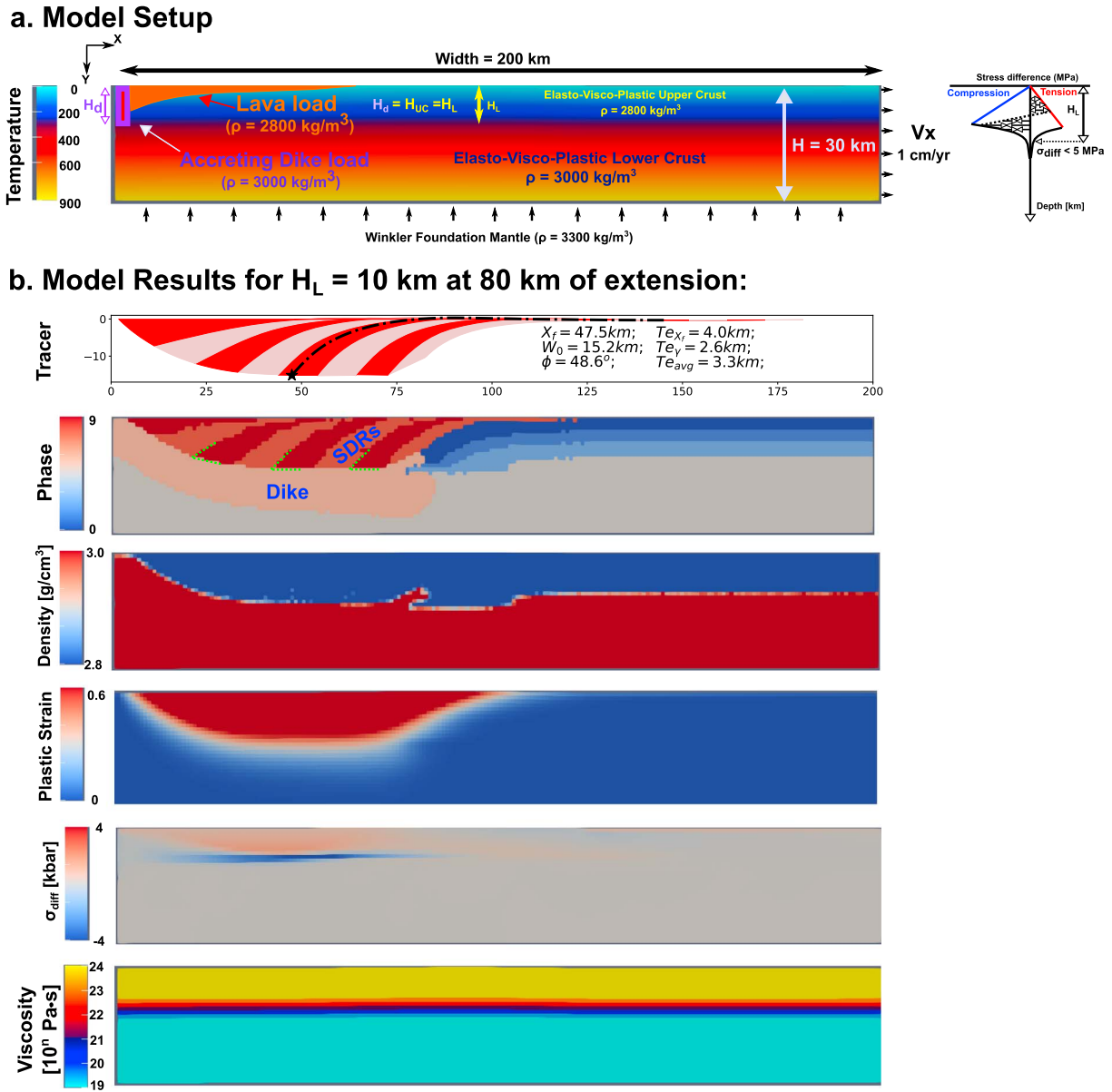
Figure 6. Model results for an elasto-visco-plastic thick plate case with constant thermal structure and Newtonian dry quartz rheology. (a) Model setup: The viscosity structure is a function of temperature that linearly increases from surface to bottom and is laterally uniform. (b) Model results for a case with a bottom boundary temperature of 900 °C that gives $H_L = 10$ km. $\phi = 48.6°$. SDR = seaward dipping reflector.

Changing the rheology from dry quartz to dry plagioclase effectively increases the lithospheric thickness H_L (Figure 9) from 16 to 28 km (no underplating) and 14 to 23 km (with underplating). Because T_e and H_L again share linear relationship that T_e is about 38% of H_L, the change of rheology also increases T_e. Note that the linear relation between T_e and H_L for the EVP thermally evolving model lies in between EP and EVP models with constant thermal structure (Figure 10). We use this relation for the mapping between T_e and H_L in data as described below.

We also study the effects of underplating. With the same model setup except for whether there is lower crustal intrusion or not, the models show different SDRs shapes. The models with underplating (Figure 9) have thinner SDRs and relatively higher T_e compared to that of the models without underplating. The models with underplating also have lower H_L than models without underplating. The extra intrusion from underplating brings in more heat and leads to a slightly weaker lithosphere (lower H_L). On the other hand,
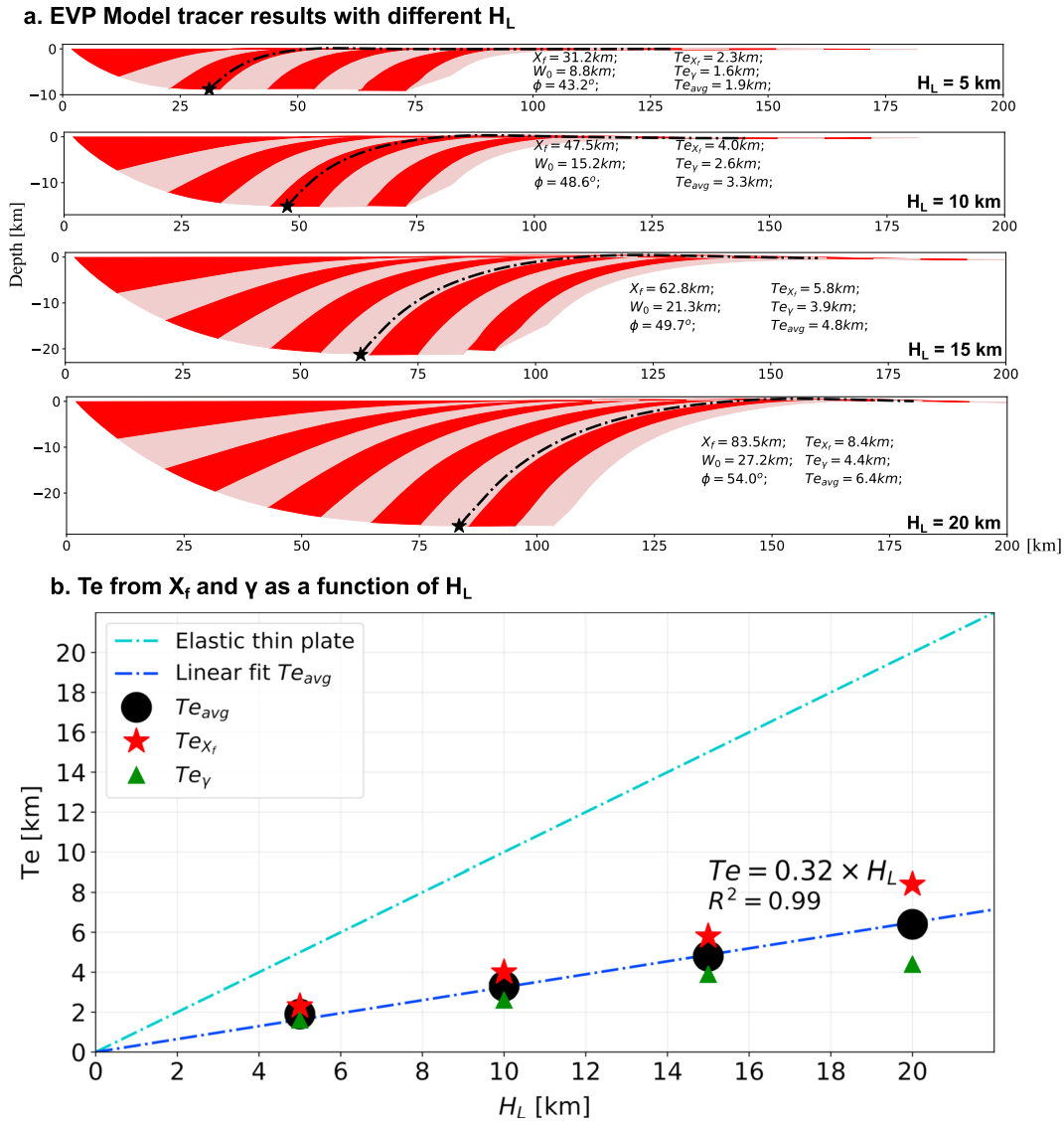
Figure 7. Model tracer results from Newtonian elasto-visco-plastic cases. (a) Seaward dipping reflector geometries with different values of H_L. (b) Effective T_e versus lithospheric thickness H_L. The red stars are T_e estimated from X_f measurements, the green triangles are from γ measurements from the models, and the black dots are the average of the two estimations. The blue dashed line is the best linear fit ($T_e = 0.32H_L$ with $R^2 = 0.99$) to the average T_e (black dots) that passes the origin.

when there is no underplating, SDRs subside faster and the increased rate of downward advection of cool material results in higher H_L. Without underplating, the model resembles the EVP constant thermal structure models (Figures 6 and 7) and the magmatic loads are compensated in the lower crust. With underplating, the lower crustal intrusion takes up the space for SDRs to subside and mantle partially becomes the compensating layer depending on how strong the crust and mantle are coupled. For strong crust-mantle coupling (as they are here for dry plagioclase), the lower crustal intrusion acts as a bridge for mantle to fully compensate the magmatic loads and this leads to a 49% reduction in SDRs thickness and 22% increase in T_e than that for models with compensation in the lower crust. For our results where crust and mantle are partially coupled, the lower crustal intrusion is "squeezed" out by the subsiding magmatic loading (dry quartz). This "squeezing" behavior induces resistance to the SDRs subsidence and causes 29% reduction in SDRs thickness and 12% increase in T_e. Despite the complexity induced by underplating, namely, decreasing H_L and increasing T_e, the T_e estimations derived from the two observables (X_f and γ) are still consistent with each other and the results fall within the narrow range of EP thick plate and EVP thick plate cases (Figure 10). This means that the effects of underplating to X_f and γ are not weighted

a. Model Setup

b. Dry Quartz without underplating:
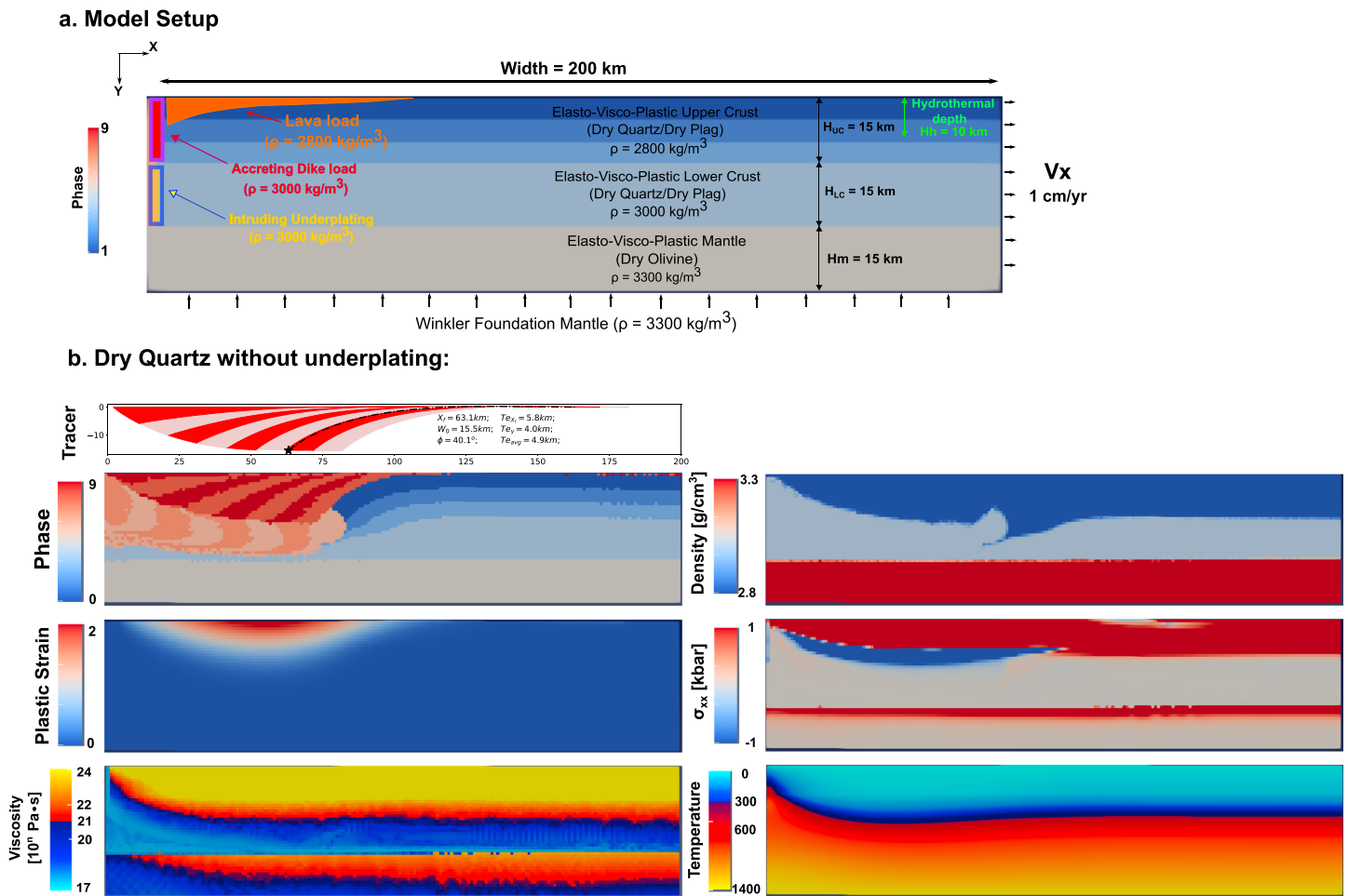
Figure 8. Elasto-visco-plastic thick plate with thermal evolution and effects of underplating. (a) Model setup: Upper crust 15 km thick with density of 2,800 kg/m³ underlying lower crust 15 km thick with a density of 3,000 kg/m³ and 15-km-thick mantle of density 3,300 kg/m³ and rheology of dry olivine (Goetze & Poirier, 1978). Model domain is 45 km thick and 200 km wide. Bottom boundary is supported by Winkler foundation with mantle density of 3,300 kg/m³. The left boundary is fixed with one column of widening dike with viscosity of 1e17 Pa·s simulating a broken plate condition. The accreting solidified dike has a density of 3,000 kg/m³ and provides a downward load near the rift axis. The right boundary is stretched with half spreading rate of $V_x = 1$ cm/year. The hydrothermal circulation is approximated with enhanced conductivity via Nusselt number described in text. Lava is filled according to the surface deflections. (b) Model results at 80 km of extension with dry quartz rheology and without underplating.

significantly differently. Thus, even with underplating, it is still valid to use the average T_e derived from X_f and γ to estimate H_L from T_e. When information about underplating and the degree of crust-mantle coupling is available, slight adjustments would yield more accurate estimations: decrease H_L by 12% for partial crust-mantle coupling to 18% for fully coupled crust and mantle.

We summarize all the model results in Figure 10. (Model parameters are summarized in Table S3; model videos are uploaded on https://doi.org/10.6084/m9.figshare.4573510.v1 website). EP thick plate models with long-term extension show a linear relationship of $T_e = 0.49 H_L$. Increasing cohesion from 20 to 40 MPa induces little increase in plate strength. EVP thick plate models with Newtonian rheology and constant thermal structure realistically simulate the density structure evolution by allowing low-density roots in the denser lower crust. Concerning effective plate strength, EVP constant thermal models predict $T_e = 0.32 H_L$. The EVP thermally evolving models fall in between with $T_e = 0.38 H_L$.

3. Analysis of Data

The major goal of this study is to link the seismically observed SDR geometries to lithospheric thickness H_L. Previous sections build a framework for achieving this goal. Essentially, the analytic model (Analytic Elastic

a. Model results with thermal evolution

b. Te from X_f and γ as a function of H_L
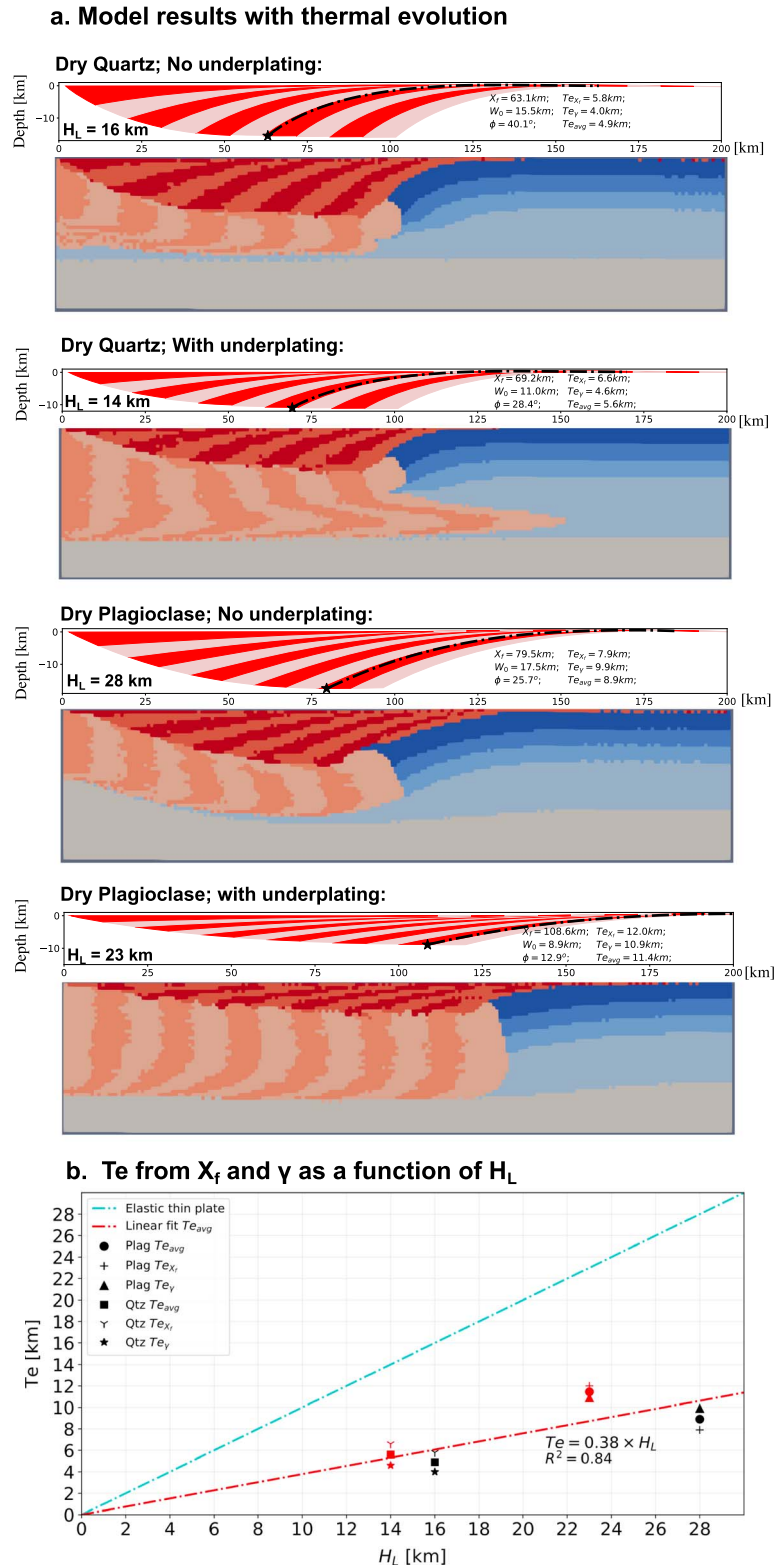
Figure 9. Thermally evolving model results summary. (a) Seaward dipping reflector geometries and phase distribution with the indicated lower crustal rheology both with and without intrusion into the lower crust (underplating). (b) Effective T_e versus lithospheric thickness H_L. The red color symbols are for models with underplating, and the black color symbols are for models without underplating. The red dashed line is the best linear fit ($T_e = 0.38 H_L$ with $R^2 = 0.84$) to the average T_e (circles and squares) that passes the origin.
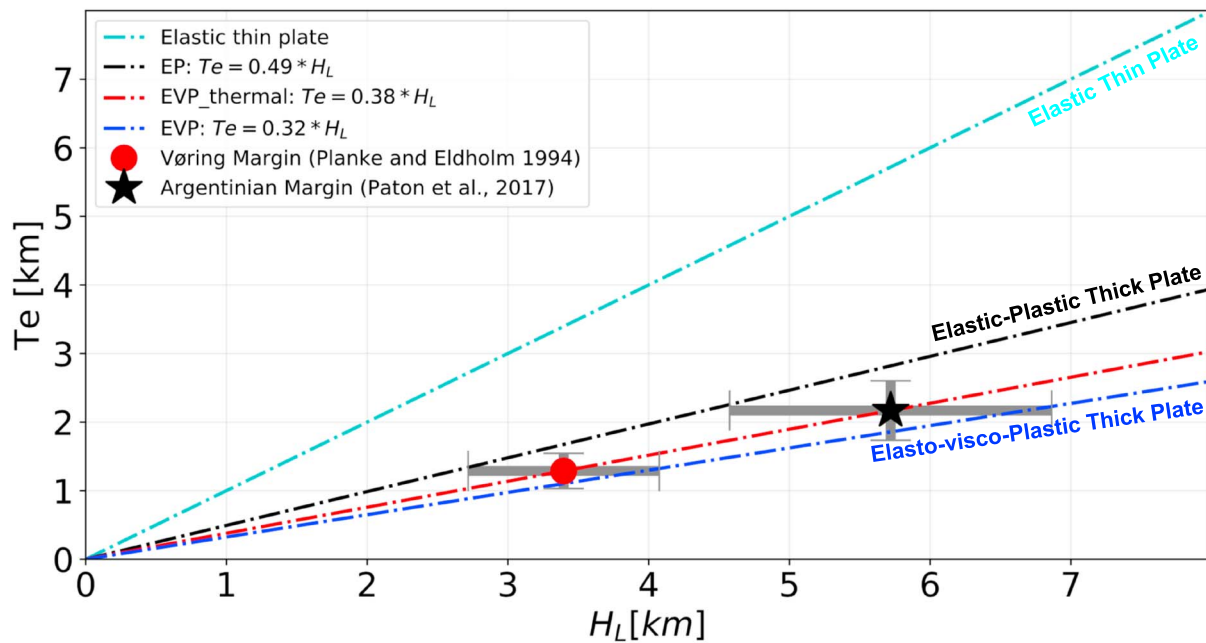
Figure 10. Final model results compilation: Mapping effective T_e to lithospheric thickness H_L. Two depth-converted images from the Vøring margin (Planke & Eldholm, 1994) and the Argentinian margin (Paton et al., 2017) are shown with error estimation as described in the text and illustrated in Figure 3. EP = elastic-plastic; EVP = elasto-visco-plastic.

Thin Plate) indicates X_f and γ are two useful and observable parameters that can be related to the effective elastic thickness T_e in both models and data. Numerical models build a quantitative relationship between T_e and H_L. Using this relationship and measuring X_f and γ from real SDRs, we can quantify the lithospheric thickness for volcanic rifted margins. When considering the three-dimensional nature of rifting, the dip angle of SDR for calculating γ is assumed to be the true dip in our 2-D cross-sectional models. However, if the strike of the data profile is not parallel to the spreading direction, the apparent dip measured is smaller than the true dip. But the effect is small for profiles away from fracture zones according to McDermott et al. (2018).

For the numerical model results, in order to estimate T_e and H_L with minimum subjective bias, we automate the data processing for retrieving the values of X_f and γ. We first estimate X_f by finding the distance from the seaward end of the SDRs to where there is a transition from negative to positive slope of the dike-lava interface. Then we find the reflecting layer intersecting the dike-lava interface at X_f, from which we calculate the dip angle ϕ at the tip of the SDR. The thickness of the SDR package at $x = X_f$ is w_0 and γ is the ratio between w_0 and $\tan(\phi)$. We take the average of T_e from X_f and γ.

Because the EVP thermally evolving models have the least assumptions, we use its derived T_e-H_L relationship for mapping T_e to H_L in data. The approach is justified because the geometry of the numerical model SDRs is very similar to that predicted by the analytic model. Thus, we use the parameters X_f and γ to estimate the value of T_e that describes the numerical model geometry. The lithospheric layer thickness H_L is taken to be the depth below the surface where the horizontal deviatoric stress decreases to 5 MPa. We then use this T_e to H_L mapping, to relate the T_e values estimated from the seismic sections with SDRs to the lithospheric thickness of plate margins at the time of rifting. From the analytic thin plate models, we analyze two depth-converted SDR profiles to yield effective elastic thickness T_e of 1.3 and 2.2 km for Vøring Margin (Figure S5) and Argentinian Margin (Figure S6), which are then mapped to lithospheric thickness during rifting of 3.4 and 5.7 km (Figure 10).

4. Discussion and Conclusions

In this paper we considered how fairly simple magmatic processes might produce the observed geometry of SDRs at volcanic rifted margins and then showed how such geometries depend on lithospheric

thickness. The basic assumption is that the "space" or depression that is filled by lava is generated by the load of solidifying magmatic intrusions and extrusives. Based on a recent published analytic description of SDR geometry, we further derived three observable parameters and showed that these parameters, relating to the width, thickness and dip of the analytic model SDRs, are functions of the effective elastic thickness T_e. The same parameters can be measured from seismic images of real SDRs. We went on to show how these geometric parameters could be used to constrain lithospheric thickness at the time of volcanic rifting.

We quantify the effects of simplifying approximations used in the analytic model on the model geometry. We first described a numerical thin elastic plate model with more realistic spatial distribution of lava flows compared to the analytic model. For the same value of T_e more reasonable lava distribution produced a ~20% larger X_f, an ~5% larger γ, and negligible change in ϕ.

We went on to develop the first two-dimensional thermal-mechanical models that simulate the geometry of SDRs formed by magmatic loads. The model allowed us to show that the thin elastic plate assumption had a modest effect on the model geometry. But, before we could do that, a thorough study of the effect of numerical grid size and time steps had to be undertaken. We also showed that the use of tracers of volcanic layers greatly increased the reliability of model predicted structures. A test of a purely elastic layer against the NTP model counterpart shows that resulting geometric differences were negligible.

Following the benchmark, we develop the 2-D models with realistic rheology and we summarize the model results in Figure 10. EP thick plate models with long-term extension show close to linear trend of $T_e = 0.49H_L$. Increasing cohesion from 20 to 40 MPa induces little increase in plate strength. EVP thick plate models with Newtonian rheology and constant thermal structure realistically calculate density structure evolution and predict a mapping of $T_e = 0.32H_L$. Effective plate strengths of the thermal evolving models fall between the narrow range of EP and EVP constant thermal model and predicts that the effective elastic thickness of the lithosphere is 38% of the actual thickness. Changing crustal material from dry quartz to dry plagioclase increases H_L and T_e by ~60%. Underplating reduces SDRs thickness by ~29% (dry quartz without crust-mantle coupling) and ~49% (dry plagioclase with crust-mantle coupling). Using the two observable parameters X_f and γ is still viable even for non-linear thermally evolving models and show consistent results.

From an analytic elastic thin plate model formulation, we derive T_e-dependent observables X_f and γ that can be directly measured in MCS data. For SDRs that have not reached steady state deflection, we consider another observable ϕ that represents the relationship between plate strength and dike loads. ϕ is useful because it is almost extension independent; namely, ϕ remains nearly constant during SDRs evolution as long as plate strength remains the same. Measuring thickness between the bottom of SDRs package and the Moho depth gives an approximation of dike height h_d. Using ϕ and h_d together we can estimate T_e. When all three observables are available for the data, calculating T_e separately from each observable gives confidence in the results. For example, from a depth-converted SDRs profile offshore Argentina at 35° south (Figure 1), X_f measurement gives $T_e = 2.2$ km, and γ results in a T_e of 2.1 km. Given the uncertainties in the MCS data, these results are highly consistent with each other.

The results indicate that the thickness of rifting lithosphere inversely correlates with estimated mantle potential temperature (T_p) of corresponding large igneous province (LIP). Based on petrological analysis, Herzberg and Gazel (2009) estimate that for North Atlantic Igneous Province the values of T_p is ~1650 °C. Our estimate of the lithospheric thickness at the time of rifting was 3.4 km. For the Paraná-Etendeka LIP Hawkesworth et al. (2000) estimate that T_p is ~1450 °C. In the nearby Argentinian basin, we find that the lithospheric thickness at the time of rifting was 5.7 km. This suggests that the hotter the mantle under an LIP the thinner the adjacent lithosphere during rifting.

Many questions about the formation of volcanic rifted margins remain. These include whether the formation of some SDRs is affected by large-offset normal faulting; what inner and outer SDRs imply about temporal and spatial variations in magmatism and crustal structures (Franke et al., 2010; McDermott et al., 2018); and how subaerially formed SDRs subside significantly below current sea level. We hope the methods developed here and the results of our analysis of lithospheric strength during rifting will aid in future efforts to resolve some of these questions.

References

Abdelmalak, M. M., Meyer, R., Planke, S., Faleide, J. I., Gernigon, L., Frieling, J., et al. (2016). Pre-breakup magmatism on the Vøring margin: Insight from new sub-basalt imaging and results from ocean drilling program hole 642E. *Tectonophysics*, *675*, 258–274. https://doi.org/10.1016/j.tecto.2016.02.037

Artemieva, I. (2011). *The lithosphere: An interdisciplinary approach*. New York: Cambridge University Press. https://doi.org/10.1017/CBO9780511975417

Becker, K., Tanner, D. C., Franke, D., & Krawczyk, C. M. (2016). Fault-controlled lithospheric detachment of the volcanic southern South Atlantic rift. *Geochemistry, Geophysics, Geosystems*, *17*, 887–894. https://doi.org/10.1002/2015GC006081

Behn, M. D., & Ito, G. (2008). Magmatic and tectonic extension at mid-ocean ridges: 1. Controls on fault characteristics. *Geochemistry, Geophysics, Geosystems*, *9*, Q08O10. https://doi.org/10.1029/2008GC001965

Bialas, R. W., Buck, W. R., & Qin, R. (2010). How much magma is required to rift a continent? *Earth and Planetary Science Letters*, *292*(1–2), 68–78. https://doi.org/10.1016/j.epsl.2010.01.021

Bodvarsson, G., & Walker, G. P. L. (1964). Crustal drift in Iceland. *Geophysical Journal of the Royal Astronomical Society*, *8*(3), 285–300. https://doi.org/10.1111/j.1365-246X.1964.tb06295.x

Brace, W. F., & Kohlstedt, D. L. (1980). Limits on lithospheric stress imposed by laboratory experiments. *Journal of Geophysical Research*, *85*(B11), 6248–6252. https://doi.org/10.1029/JB085iB11p06248

Buck, W. R. (2006). The role of magma in the development of the afro-Arabian rift system. *Geological Society, London, Special Publications*, *259*(1), 43–54. https://doi.org/10.1144/GSL.SP.2006.259.01.05

Buck, W. R. (2017). The role of magmatic loads and rift jumps in generating seaward dipping reflectors on volcanic rifted margins. *Earth and Planetary Science Letters*, *466*, 62–69. https://doi.org/10.1016/j.epsl.2017.02.041

Buck, W. R., Lavier, L. L., & Poliakov, A. N. B. (2005). Modes of faulting at mid-ocean ridges. *Nature*, *434*(7034), 719–723. https://doi.org/10.1038/nature03358

Buiter, S. J. H., & Torsvik, T. H. (2014). A review of Wilson cycle plate margins: A role for mantle plumes in continental break-up along sutures? *Gondwana Research*, *26*(2), 627–653. https://doi.org/10.1016/j.gr.2014.02.007

Calvès, G., Schwab, A. M., Huuse, M., Clift, P. D., Gaina, C., Jolley, D., et al. (2011). Seismic volcanostratigraphy of the western Indian rifted margin: The pre-Deccan igneous province. *Journal of Geophysical Research*, *116*, B01101. https://doi.org/10.1029/2010JB000862

Choi, E., Buck, W. R., Lavier, L. L., & Petersen, K. D. (2013). Using core complex geometry to constrain fault strength. *Geophysical Research Letters*, *40*, 3863–3867. https://doi.org/10.1002/grl.50732

Choi, E., Lavier, L., & Gurnis, M. (2008). Thermomechanics of mid-ocean ridge segmentation. *Physics of the Earth and Planetary Interiors*, *171*(1–4), 374–386. https://doi.org/10.1016/j.pepi.2008.08.010

Comer, R. P. (1983). Thick plate flexure. *Geophysical Journal International*, *72*(1), 101–113. https://doi.org/10.1111/j.1365-246X.1983.tb02807.x

Courtillot, V., Jaupart, C., Manighetti, I., Tapponnier, P., & Besse, J. (1999). On causal links between flood basalts and continental breakup. *Earth and Planetary Science Letters*, *166*(3–4), 177–195. https://doi.org/10.1016/S0012-821X(98)00282-9

Cundall, P. A. (1989). Numerical experiments on localization in frictional materials. *Ingenieur Archiv*, *59*(2), 148–159. https://doi.org/10.1007/BF00538368

Davis, J. K., & Lavier, L. L. (2017). Influences on the development of volcanic and magma-poor morphologies during passive continental rifting. *Geosphere*, *13*(5), 1524–1540. https://doi.org/10.1130/GES01538.1

Direen, N. G., & Crawford, A. J. (2003). Fossil seaward-dipping reflector sequences preserved in southeastern Australia: A 600 Ma volcanic passive margin in eastern Gondwanaland. *Journal of the Geological Society*, *160*(6), 985–990. https://doi.org/10.1144/0016-764903-010

Ebinger, C. J., & Hayward, N. J. (1996). Soft plates and hot spots: Views from Afar. *Journal of Geophysical Research*, *101*(B10), 21,859–21,876. https://doi.org/10.1029/96JB02118

Eldholm, O., Skogseid, J., Planke, S., & Gladczenko, T. P. (1995). Volcanic Margin Concepts. In *Rifted Ocean-Continent Boundaries* (pp. 1–16). Dordrecht, Netherlands: Springer. https://doi.org/10.1007/978-94-011-0043-4_1

Elliott, G. M., Berndt, C., & Parson, L. M. (2009). The SW African volcanic rifted margin and the initiation of the Walvis Ridge, South Atlantic. *Marine Geophysical Researches*, *30*(3), 207–214. https://doi.org/10.1007/s11001-009-9077-x

Franke, D., Ladage, S., Schnabel, M., Schreckenberger, B., Reichert, C., Hinz, K., et al. (2010). Birth of a volcanic margin off Argentina, South Atlantic. *Geochemistry, Geophysics, Geosystems*, *11*, Q0AB04. https://doi.org/10.1029/2009GC002715

Geoffroy, L. (2005). Volcanic passive margins. *Comptes Rendus Geoscience*, *337*(16), 1395–1408. https://doi.org/10.1016/j.crte.2005.10.006

Geoffroy, L., Burov, E. B., & Werner, P. (2015). Volcanic passive margins: Another way to break up continents. *Scientific Reports*, *5*, 14828. https://doi.org/10.1038/srep14828

Gibson, I. L., & Love, D. (1989). A listric fault model for the formation of the dipping reflectors penetrated during the drilling of Hole 642E, ODP Leg 104. In O. Eldholm, J. Thiede, E. Taylor, et al. (Eds.), *Proc. ODP, Sci. Results* (Vol. 104, pp. 979–983). College Station, TX: Ocean Drilling Program. https://doi.org/10.2973/odp.proc.sr.104.195.1989

Gladczenko, T. P., Skogseid, J., & Eldhom, O. (1998). Namibia volcanic margin. *Marine Geophysical Researches*, *20*(4), 313–341. https://doi.org/10.1023/A:1004746101320

Goetze, C., & Poirier, J. P. (1978). The mechanisms of creep in olivine [and discussion]. *Philosophical Transactions of the Royal Society A: Mathematical, Physical and Engineering Sciences*, *288*(1350), 99–119. https://doi.org/10.1098/rsta.1978.0008

Hawkesworth, C. J., Gallagher, K., Kirstein, L., Mantovani, M. S. M., Peate, D. W., & Turner, S. P. (2000). Tectonic controls on magmatism associated with continental break-up: An example from the Paraná–Etendeka Province. *Earth and Planetary Science Letters*, *179*(2), 335–349. https://doi.org/10.1016/S0012-821X(00)00114-X

Herzberg, C., & Gazel, E. (2009). Petrological evidence for secular cooling in mantle plumes. *Nature*, *458*(7238), 619–622. https://doi.org/10.1038/nature07857

Hinz, K (1981). A hypothesis on terrestrial catastrophes—Wedges of very thick Oceanward Dipping Layers beneath Passive Continental Margi.pdf. Retrieved from http://www.schweizerbart.de/publications/detail/artno/186082200/A-Hypothesis-on-Terrestrial-Catastrophes

Jackson, M. P., Cramez, C., & Fonck, J.-M. (2000). Role of subaerial volcanic rocks and mantle plumes in creation of South Atlantic margins: Implications for salt tectonics and source rocks. *Marine and Petroleum Geology*, *17*(4), 477–498. https://doi.org/10.1016/S0264-8172(00)00006-4

Kalberg, T., & Gohl, K. (2014). The crustal structure and tectonic development of the continental margin of the Amundsen Sea embayment, West Antarctica: Implications from geophysical data. *Geophysical Journal International*, *198*(1), 327–341. https://doi.org/10.1093/gji/ggu118

Kendall, J.-M., Stuart, G. W., Ebinger, C. J., Bastow, I. D., & Keir, D. (2005). Magma-assisted rifting in Ethiopia. *Nature*, *433*(7022), 146–148. https://doi.org/10.1038/nature03161

Kristoffersen, Y., Hofstede, C., Diez, A., Blenkner, R., Lambrecht, A., Mayer, C., & Eisen, O. (2014). Reassembling Gondwana: A new high quality constraint from vibroseis exploration of the sub-ice shelf geology of the East Antarctic continental margin. *Journal of Geophysical Research: Solid Earth*, *119*, 9171–9182. https://doi.org/10.1002/2014JB011479

Lavier, L. L., & Buck, W. R. (2002). Half graben versus large-offset low-angle normal fault: Importance of keeping cool during normal faulting. *Journal of Geophysical Research*, *107*(B6), 2122. https://doi.org/10.1029/2001JB000513

McDermott, C., Lonergan, L., Collier, J. S., McDermott, K. G., & Bellingham, P. (2018). Characterization of seaward-dipping reflectors along the S. American Atlantic margin and implications for continental breakup. *Tectonics*, *37*, 3303–3327. https://doi.org/10.1029/2017TC004923

Morgan, R., & Watts, A. (2018). Seismic and gravity constraints on flexural models for the origin of seaward dipping reflectors. *Geophysical Journal International*, *214*(3), 2073–2083. https://doi.org/10.1093/gji/ggy243

Mutter, J. C., Talwani, M., & Stoffa, P. L. (1982). Origin of seaward-dipping reflectors in oceanic crust off the Norwegian margin by "subaerial sea-floor spreading". *Geology*, *10*(7), 353. https://doi.org/10.1130/0091-7613(1982)10<353:OOSRIO>2.0.CO;2

Olive, J.-A., Behn, M. D., Mittelstaedt, E., Ito, G., & Klein, B. Z. (2016). The role of elasticity in simulating long-term tectonic extension. *Geophysical Journal International*, *205*(2), 728–743. https://doi.org/10.1093/gji/ggw044

Palmason, G. (1973). Kinematics and heat flow in a volcanic rift zone, with application to Iceland. *Geophysical Journal International*, *33*(4), 451–481. https://doi.org/10.1111/j.1365-246X.1973.tb02379.x

Paton, D. A., Pindell, J., McDermott, K., Bellingham, P., & Horn, B. (2017). Evolution of seaward-dipping reflectors at the onset of oceanic crust formation at volcanic passive margins: Insights from the South Atlantic. *Geology*, G38706.1. https://doi.org/10.1130/G38706.1

Pérez-Gussinyé, M., Lowry, A. R., & Watts, A. B. (2007). Effective elastic thickness of South America and its implications for intracontinental deformation. *Geochemistry, Geophysics, Geosystems*, *8*, Q05009. https://doi.org/10.1029/2006GC001511

Pindell, J., Graham, R., & Horn, B. (2014). Rapid outer marginal collapse at the rift to drift transition of passive margin evolution, with a Gulf of Mexico case study. *Basin Research*, *26*(6), 701–725. https://doi.org/10.1111/bre.12059

Planke, S., & Eldholm, O. (1994). Seismic response and construction of seaward dipping wedges of flood basalts: Vøring volcanic margin. *Journal of Geophysical Research*, *99*(B5), 9263–9278. https://doi.org/10.1029/94JB00468

Planke, S., Symonds, P. A., Alvestad, E., & Skogseid, J. (2000). Seismic volcanostratigraphy of large-volume basaltic extrusive complexes on rifted margins. *Journal of Geophysical Research*, *105*(B8), 19,335–19,351. https://doi.org/10.1029/1999JB900005

Qin, R., & Buck, W. R. (2008). Why meter-wide dikes at oceanic spreading centers? *Earth and Planetary Science Letters*, *265*(3-4), 466–474. https://doi.org/10.1016/j.epsl.2007.10.044

Quirk, D. G., Shakerley, A., & Howe, M. J. (2014). A mechanism for construction of volcanic rifted margins during continental breakup. *Geology*, *42*(12), 1079–1082. https://doi.org/10.1130/G35974.1

Saikia, U., Das, R., & Rai, S. S. (2017). Possible magmatic underplating beneath the west coast of India and adjoining Dharwar craton: Imprint from Archean crustal evolution to breakup of India and Madagascar. *Earth and Planetary Science Letters*, *462*, 1–14. https://doi.org/10.1016/j.epsl.2017.01.004

Shelton, G. L., & Tullis, J. (1981). Experimental flow laws for crustal rocks. *Eos, Transactions of the American Geophysical Union*, *62*, 396. Retrieved from http://ci.nii.ac.jp/naid/10010125720/en/

Tian, X., & Choi, E. (2017). Effects of axially variable diking rates on faulting at slow spreading mid-ocean ridges. *Earth and Planetary Science Letters*, *458*, 14–21. https://doi.org/10.1016/j.epsl.2016.10.033

Watts, A. B., & Cox, K. G. (1989). The Deccan traps: An interpretation in terms of progressive lithospheric flexure in response to a migrating load. *Earth and Planetary Science Letters*, *93*(1), 85–97. https://doi.org/10.1016/0012-821X(89)90186-6

White, R. S., Smith, L. K., Roberts, A. W., Christie, P. A. F., Kusznir, N. J., Roberts, A. M., et al. (2008). Lower-crustal intrusion on the North Atlantic continental margin. *Nature*, *452*(7186), 460–464. https://doi.org/10.1038/nature06687